

Article

Oxide-Clay Mineral as Photoactive Material for Dye Discoloration

Maicon O. Miranda ¹, Bartolomeu Cruz Viana ², Luzia Maria Honório ², Pollyana Trigueiro ², Maria Gardênnia Fonseca ³, Francisco Franco ⁴, Josy A. Osajima ^{2,*} and Edson C. Silva-Filho ^{2,*}

¹ Instituto Federal do Piauí, Campus Cocal, Cocal, Piauí 64235-000, Brazil; maikon008@hotmail.com

² Laboratório Interdisciplinar de Materiais Avançados (LIMAV), UFPI, Teresina, Piauí 64049-550, Brazil; bartolomeu@ufpi.edu.br (B.C.V.); luzia_quimica@yahoo.com.br (L.M.H.); pollyanatrigueiro@gmail.com (P.T.)

³ Núcleo de Pesquisa e Extensão-Laboratório de Combustíveis e Materiais (NPE-LACOM), UFPB, João Pessoa, Paraíba 58051-970, Brazil; mgardennia@gmail.com

⁴ Departamento de Química Inorgánica, Cristalografía y Mineralogía Facultad de Ciencias, Universidad de Málaga Campus de Teatinos s/n, 29071 Málaga, Spain; ffranco@uma.es

* Correspondence: josyosajima@ufpi.edu.br (J.A.O.); edsonfilho@ufpi.edu.br (E.C.S.-F.); Tel.: +55-86-32215710 (E.C.S.-F.)

Received: 2 December 2019; Accepted: 22 January 2020; Published: 1 February 2020



Abstract: Titanium and zirconium oxides (TiO₂ and ZrO₂, respectively) were obtained from alkoxides hydrolyses, and then deposited into palygorskite clay mineral (Pal) to obtain new materials for photocatalytic applications. The obtained materials were characterized by structural, morphological, and textural techniques. X-ray diffraction (XRD) results confirmed the characteristic peaks of oxides and clay transmission electron microscopy (TEM) and scanning electron microscopy (SEM) images of the modified palygorskite with both oxides showed that the clay was successfully modified by the proposed method. The increase in the specific surface area of the clay occurred when TiO₂ and ZrO₂ were deposited on the surface. The photocatalytic activity of these materials was investigated using the Remazol Blue anion dye under UV light. The evaluated systems presented high photocatalytic activity, reaching approximately 98% of dye discoloration under light. Thus, TiO₂-Pal and ZrO₂-TiO₂-Pal are promising clay mineral-based photocatalysts.

Keywords: TiO₂; ZrO₂; palygorskite; support; photocatalytic process

1. Introduction

The substantial use of chemical compounds is essential to achieve the social and economic goals of the global community, and current best practices demonstrate that they can be widely used in a cost-effective manner and with a high degree of safety. However, much remains to be done to ensure the environmentally friendly use of toxic chemicals within the principles of sustainable development and to improve the quality of life of humankind [1,2].

Particularly in developing countries, two of the major problems are: (1) the lack of scientific data to assess the risks associated with the use of numerous chemicals and (2) the lack of resources to assess chemicals for which data are available [3,4]. Researchers and government entities are exploring solutions to mitigate the large amount of pollutants released into the environment, including textile dyes, which, despite their toxicity, are still released into bodies of water without prior treatment [5,6]. Dyes can be removed from the environment through easily attainable, low-cost techniques; advanced oxidative processes (AOPs) deserve special attention among these techniques [7,8].

Currently, systematic work on dye removal from textile effluents has been extensively proposed [9,10], as it is a type of waste that is highly targeted by inspection agencies due to its physical and chemical characteristics. Adsorption, precipitation, filtration, and biological and chemical degradations are the most common techniques for water treatment. AOPs, also termed chemical degradation, have been studied because these processes are destructive and have the advantage of not generating solid residues reaching mineralization levels for many organic pollutants [11,12].

Most AOPs occur at room temperature, using energy to produce highly reactive intermediates with high oxidation or reduction potential. The process can attack and destroy hazardous compounds [13,14] and generate free radicals such as hydroxyl (OH), which is a very effective oxidizing agent. Both research and application studies on AOPs, especially heterogeneous photocatalysis, have increased every year and are becoming of fundamental importance in environmental chemistry [15,16].

Diverse toxic organic compound classes are susceptible to degradation using heterogeneous photocatalysis. This process promotes the total mineralization of the pollutants, generating CO₂, H₂O, and ionic compounds [17,18]. Some classes of compounds susceptible to degradation by photocatalysis are alkanes, chloroaliphatics, azo compounds, alcohols, carboxylic acids, phenols, chlorophenols, herbicides, surfactants, and dyes [19–22].

In heterogeneous photocatalytic reactions, inorganic semiconductors are generally used due to the characteristics of electronic structures, such as an energy gap [23,24]. Besides, these compounds have high physicochemical stability and can be immobilized on substrates or dispersed in the solution, thereby facilitating their separation after catalysis [25]. For example, titanium and zirconium oxides (TiO₂ and ZrO₂, respectively) act as catalysts and have a high degradation efficiency.

TiO₂ is an efficient photocatalytic semiconductor for environmental applications owing to its low toxicity, high oxidation power, high corrosion resistance, and activation capacity by sunlight. TiO₂ has a band gap of 3.2 eV and requires 380–400 nm for its catalytic activity. ZrO₂ presents monoclinic, tetragonal, and cubic forms and also has photocatalytic properties. Monoclinic ZrO₂ presents a band gap energy between 5.8 and 7.1 eV, but a lower value of approximately 5.2 eV has been estimated by optical absorption [26]. These oxides can also perform better in terms of photocatalytic activity by increasing their specific surface area, thereby increasing the number of active sites for chemical compound degradation. Immobilization of the oxides on a support increases their surface area. Among the most used substrates, clay minerals have drawn considerable interest owing to their low cost, availability, environmental stability, high surface area, adsorption capacity, anti-ultraviolet ray effects, and ion exchange properties [27,28].

Clay minerals have attracted attention in recent years as functional materials owing to their special and different structures, high specific surface areas, and remarkable adsorption capacities [29,30]. They can be used as alternative materials for the immobilization of compounds with photocatalytic properties [31,32]. Among the clays used, palygorskite has emerged as a promising material. Palygorskite is a magnesium-aluminum phyllosilicate with a fibrous morphology. It exhibits continuous octahedral layers in only one dimension, and periodic reversal of the tetrahedral sheets, with apical oxygen alternately pointing up and down in adjacent strands that are still attached, resulting in a porous structure the channels of which contain exchangeable cations and water molecules [19,33]. Palygorskite is usually used as a bleaching and clarifying agent, filtration medium, catalyst, adsorbent, pesticide carrier, rheological agent in drilling fluids, and after acid treatments of phosphorus compounds and oil contaminants [34,35].

Therefore, the present work aims to synthesize photoactive materials by depositing titanium and/or zirconium oxides in the palygorskite clay mineral support and investigate the discoloration of a reactive dye (Remazol Brilliant Blue R) in an aqueous medium.

2. Materials and Methods

2.1. Materials

Zirconium oxychloride ($\text{ZrOCl}_2 \cdot 8\text{H}_2\text{O}$) and titanium isopropoxide ($\text{Ti}(\text{OCH}(\text{CH}_3)_2)_4$), both from Synth, and aqueous ammonia (32%, Vetec) were used as received. Palygorskite was provided by Coimbra Company located in Guadalupe (Piauí, Brazil) and was used as received. Milli-Q water was used in all procedures.

2.2. Preparation of Photoactive Materials

2.2.1. TiO_2 -Palygorskite Composite (TiO_2 -Pal)

TiO_2 was prepared separately from the clay mineral sample. It was deposited by the slow addition (dropping) of 8.0 g of titanium isopropoxide in 100.0 mL of deionized water for titanium hydrolysis, then added into 5.0 g of palygorskite, and stirred for 4 h. Subsequently, the suspension was centrifuged at 2500 rpm for 4 min and the obtained solid was washed with deionized water five times. Then, the solid was dried at 353 K and finally calcined at 573 K for 4 h [36].

2.2.2. ZrO_2 - TiO_2 -Palygorskite Composite (ZrO_2 - TiO_2 -Pal)

ZrO_2 was deposited on a previously prepared TiO_2 -Pal sample. Here, zirconium oxychloride was initially solubilized in 15.0 mL of concentrated hydrochloric acid and added to 100.0 mL of an aqueous suspension containing 5.0 g of TiO_2 -Pal, followed by the addition of aqueous ammonia to hydrolyze the zirconium. The system was magnetically stirred for 4 h, followed by centrifugation and washing until a neutral final pH was achieved. The obtained solid was dried at 353 K and finally calcined at 573 K for 4 h at a heating rate of $1\text{ }^\circ\text{C min}^{-1}$ [36].

2.3. Characterization

The materials were characterized by X-ray diffraction (XRD) using a Shimadzu LabX XRD-600 with $\text{Cu-K}\alpha$ radiation ($\lambda = 1.5406\text{ \AA}$), 2θ in the range of 5° – 75° , a scan rate of 5° min^{-1} , and a total exposure time of 15 min. The textural properties were determined from nitrogen adsorption–desorption measurements recorded at 77 K with a Quantachrome NOVA 4200 device. Samples were previously degassed at 423 K for 15 h under vacuum (10^{-4} mbar) to ensure a clean and dry surface. The specific surface areas were calculated according to the standard BET procedure. The isotherms were registered in the range of $0.0 < P/P_0 < 1.0$. Fourier transform infrared (FTIR) absorption spectroscopy was performed using a 660-IR Varian spectrometer with KBr pellets and with 1% of the sample, in the region of 4000 – 400 cm^{-1} with a total of 92 scans and a resolution of 4 cm^{-1} . Changes in the morphology before and after deposition of the oxides were observed by scanning electron microscopy (SEM). The micrographs were obtained from a JEOL T300 microscope after plating the samples with gold and palladium. Morphological analyses of the synthesized particles were carried out by transmission electron microscopy (TEM) using a JEOL JEM-1400 device with an acceleration voltage of 120 kV (LNLS). UV-Visible diffuse reflectance spectra were obtained using a Shimadzu UV-3600 (UV-Visible Spectrophotometer) in the range of 200–800 nm to calculate the band gap of the photoactive materials.

2.4. Photodegradation Assays

2.4.1. Effects of Concentration and Time

The photocatalytic activity of the TiO_2 -Pal and ZrO_2 - TiO_2 -Pal composites was evaluated using Remazol Blue dye under UV light. The suspension was prepared using $1.0 \times 10^{-4}\text{ mol L}^{-1}$ Remazol Blue in photoactive material concentrations of 0.5–1.5 g L^{-1} . The system was placed in a radiation box equipped with a 125 W mercury lamp using UV light at 298 K. The suspension or solution was stirred at 600 rpm to maintain the homogeneity of the system. Samples were collected at predetermined times:

0.5, 15, 30, 45, 60, 90, and 120 min. Kinetic discoloration of the dye was carried out using a Shimadzu UV-3600 UV-Visible spectrophotometer at the maximum absorption wavelength of the dye (589 nm) in both the presence and absence of the photoactive material. The suspensions were centrifuged at 3500 rpm for 3 min prior to analysis.

2.4.2. Influence of the Sulfate Ion

0.1 mol L⁻¹ sulfate was used in all experiments containing 1.5 g L⁻¹ of the photoactive material. The photocatalytic activity in the presence and absence of the sulfate was monitored for 120 min.

3. Results

3.1. Characterizations

Figure 1 shows the XRD patterns of the palygorskite and the materials obtained after the deposition of TiO₂ and ZrO₂ in the starting palygorskite. Reflections of palygorskite were indexed using crystallographic records (JCPDS card no. 1-082-183). This phyllosilicate coexisted alongside a small amount of quartz, as evidenced by the diffraction reflections associated with interplanar distances of 4.26, 3.34, and 1.82 Å.

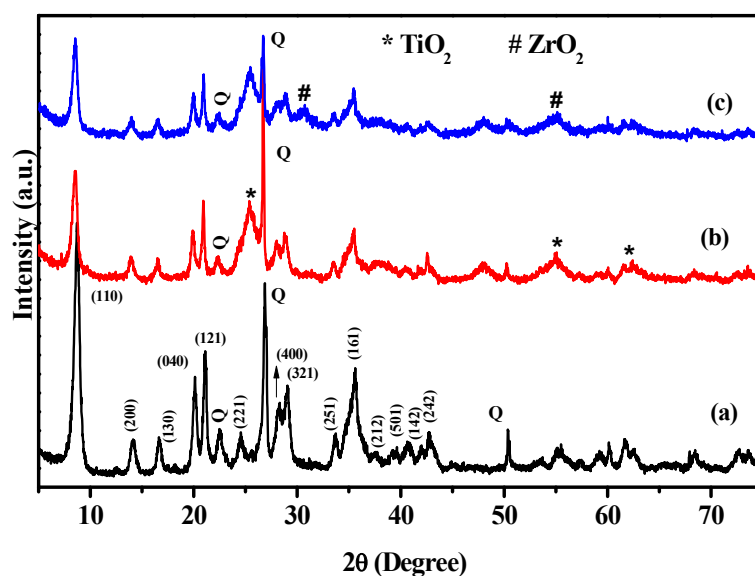


Figure 1. X-ray diffractograms for (a) Pal, (b) TiO₂-Pal, and (c) ZrO₂-TiO₂-Pal.

Figure 1b shows the XRD patterns of the TiO₂-Pal sample. During the synthesis of this new material, the treatment conditions generated the following modifications in the diffraction profile: (1) a decrease in the intensity of the 110 reflection of palygorskite with respect to the intensity of the quartz diffraction peaks, (2) a slight increase in the full width at half maximum (FWHM) of the 110 reflection, and (3) a loss of definition of 212, 501, 142, and 242 reflections between 2θ values of 35° and 45°. These aspects suggested a slight loss of crystallinity in the palygorskite structure. On the other hand, new reflections at 2θ values of 25.3°, 47.9°, and 55° were related with the 101, 220, and 211 reflections of the anatase phase, which appeared after calcination at 573 K and the deposition of TiO₂. [37]

XRD patterns for the ZrO₂-TiO₂-Pal sample (Figure 1c) showed: (1) a decrease in the intensity of the 110 reflection and a simultaneously increasing FWHM, (2) a noticeable decrease in the signal-to-noise ratio, and (3) the loss of definition of the reflection between 2θ values of 35°–45°, forming a broad signal with multiple maximums. In addition, in Figure 1b, the reflections at 2θ values of 25.3°, 47.9°, and 55° were assigned to the anatase phase. Moreover, two new reflections at 30.8° and 60.9° were attributed to the 011 and 311 planes of ZrO₂, respectively [38]. These results suggest the presence of ZrO₂ nanoparticles in the surface of palygorskite fibers.

N_2 adsorption–desorption isotherms of the Pal, TiO_2 -Pal, and ZrO_2 - TiO_2 -Pal composites are shown in Figure 2. The isotherms resembled type III, with the representative hysteresis of an H_3 -type mesoporous material [39]. A change in the hysteresis form in the P/P_0 range between 0.60 and 0.95 was observed (Figure 2B,C) for the modified solids when compared to the palygorskite hysteresis (Figure 2A). This change was associated with the presence of the oxides that contribute to a decrease in the pore size for both materials in the P/P_0 range between 0.8 and 0.95. A major difference in P/P_0 close to 0.65 was observed for TiO_2 -Pal.

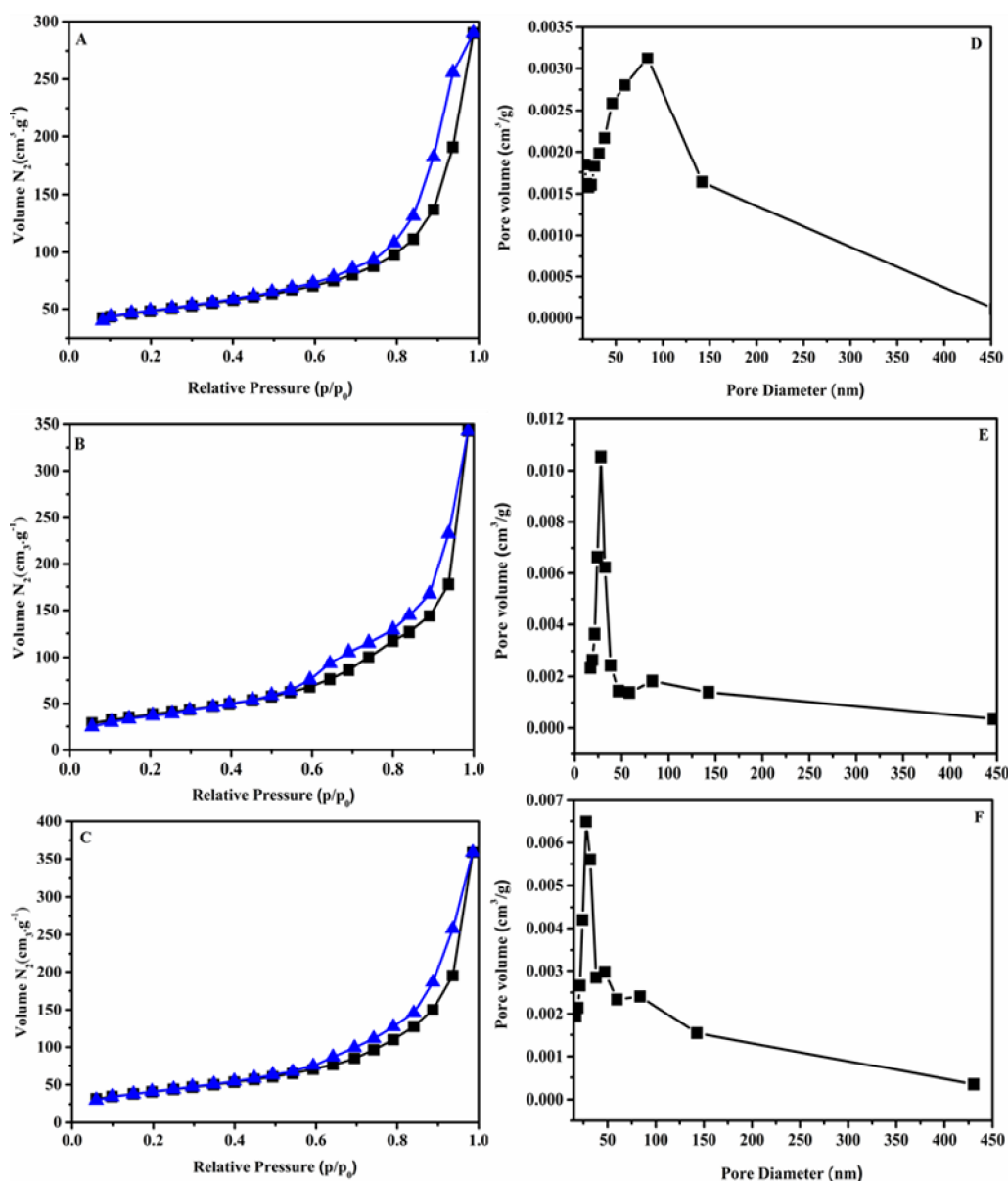


Figure 2. N_2 adsorption–desorption isotherms and pore diameter distribution for: (A,D) palygorskite; (B,E) TiO_2 -Pal; and (C,F) ZrO_2 - TiO_2 -Pal.

The specific surface area of palygorskite was $113\text{ m}^2\text{ g}^{-1}$. After TiO_2 deposition on the clay structure, the area increased to $136\text{ m}^2\text{ g}^{-1}$ and reached $146\text{ m}^2\text{ g}^{-1}$ in ZrO_2 - TiO_2 -Pal. The increase in area can be attributed to the dispersion of fine particles on the surface.

Figure 2B shows a desorption hysteresis phenomenon that is not perfectly parallel to the adsorption step, indicating a certain degree of variation in the pore diameter, as evidenced by the values obtained

from the BJH (Barrett, Joyner, and Halenda) method (Figure 2). Additionally, the adsorption appears with a gradual increase in pressure, which indicates the presence of secondary porosity [40].

The pore size distribution was calculated by the BJH method that was applied to the desorption data in Figure 2D–F and was consistent with the presence of mesopores in the composites, according to IUPAC (International Union of Pure and Applied Chemistry) classification. A pore size distribution between 20 and 100 nm was observed for the palygorskite, suggesting a presence of varied pore sizes (micro-, meso-, and macroporous) [41]. After the oxide deposition, a narrowed distribution in pore sizes was observed, and smaller pores were formed after the oxide deposition into the palygorskite [39], corroborating the results in Figure 2.

FTIR spectra of palygorskite and the obtained materials are shown in Figure 3. In the palygorskite spectrum (Figure 3a), bands at 3622 and 3534 cm^{-1} are assigned to the stretching modes of hydroxyl groups, referring to M–OH groups (M = Mg, Al, Fe) [42]. The broad bands at 3410 and 3276 cm^{-1} are characteristic of water molecules adsorbed at the outer surface of palygorskite fibers and both “zeolitic” and crystallization water located in the structure of chains aligned parallel to the a axis [43]. The band at 1661 cm^{-1} was attributed to water bending vibrations [43]. On the other hand, bands between 1100 and 900 cm^{-1} are characteristic of the Si–O–Si and Si–OH stretching modes [44].

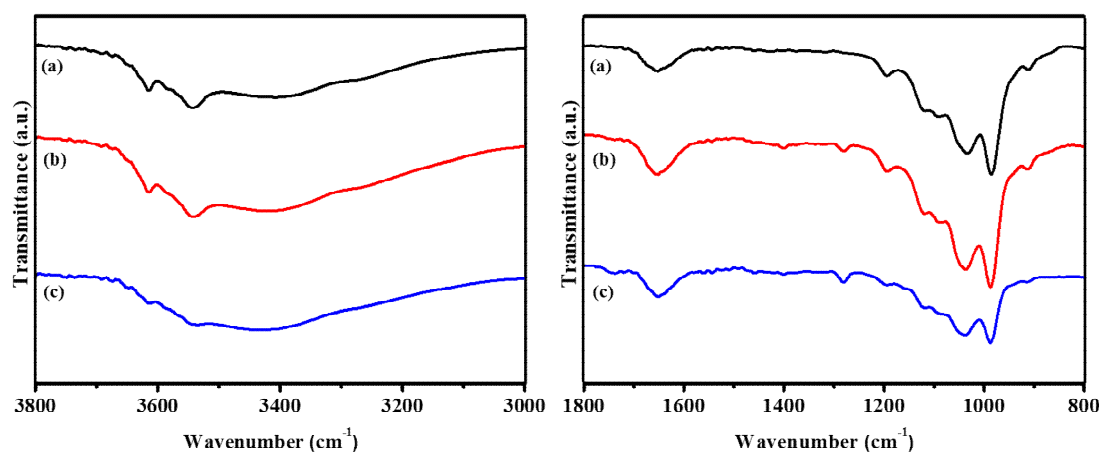


Figure 3. Infrared spectra (FTIR) of (a) Palygorskite, (b) TiO_2 -Pal, and (c) ZrO_2 - TiO_2 -Pal.

Figure 3 also shows the FTIR spectra of the obtained materials. The FTIR spectrum of the TiO_2 -Pal sample shows no changes compared with the FTIR spectrum of the palygorskite. However, ZrO_2 - TiO_2 -Pal has minor modifications related to a loss in the intensity of the bands corresponding to the stretching modes of the M–OH and Si–O–Si groups. These modifications can be related to the increase in the structural ordering as a result of the treatment conditions [45]. In the region below 1000 cm^{-1} , bands occur that refer to Zr–O, Ti–O–Ti, and Ti–O–O, but the M–O band of the clay is overlapped, and it is not possible to emphasize them.

SEM images (Figure 4a–c) show the characteristic morphology of the natural palygorskite in the form of elongated crystals and the presence of particles of TiO_2 and ZrO_2 , which were deposited in the clay structure. Compared to palygorskite (Figure 4a), the presence of the TiO_2 - and ZrO_2 -modified clay morphologies (Figure 4b,c), which show needle shapes and a porous structure, confirms that the deposition was performed successfully [46,47].

More dispersion of the Pal needles after TiO_2 deposition was also observed (Figure 4b). However, the needles are aggregated after ZrO_2 deposition (Figure 4c) when compared with precursor TiO_2 -Pal (Figure 4b), although both surfaces are more porous than the pristine palygorskite (Figure 4a); this result agrees with the textural analysis (Figure 2). TEM images (Figure 4) show particles agglomerated on the Pal needles (marked with red circles). It is important to note that Figure 4d does not show these particle agglomerates. In the SEM image, the particles cannot be observed; only a greater roughness of the Pal needles is observed, which could indicate a particle coating.

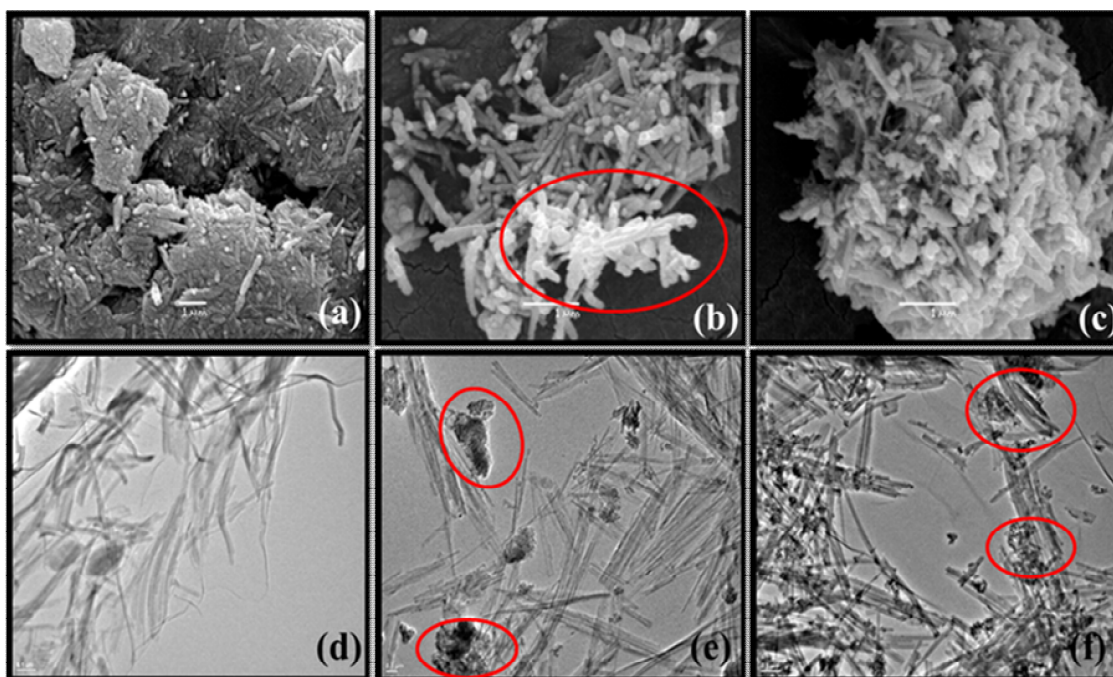


Figure 4. Scanning electron microscopy (SEM) and transmission electron microscopy (TEM) micrographs: (a,d) Palygorskite; (b,e) TiO_2 -Pal; (c,f) ZrO_2 - TiO_2 -Pal.

The transmission electron micrographs (Figure 4d–f) show the presence of needle-shaped crystals, confirming the typical fibrous structure of the clay sample (Figure 4d). After TiO_2 deposition (Figure 4e), the morphology was maintained with the presence of particle aggregates on the needle surface. In addition, the ZrO_2 - TiO_2 -Pal composite exhibited a uniform distribution of the oxide on the palygorskite surface (Figure 4f) [48].

Figure 5 shows the energy gap (E_g) values for the synthesized composites. The E_g values are close for both modified solids (3.43 eV for TiO_2 -Pal and 3.50 eV for ZrO_2 - TiO_2 -Pal), which can lead to better photocatalytic performance as the band gap energy is less than 3.5 eV. The values (shown in Figure 5) are in agreement with the 3.43 eV and 3.61 eV reported for TiO_2 -Pal and ZrO_2 - TiO_2 -Pal, respectively [49].

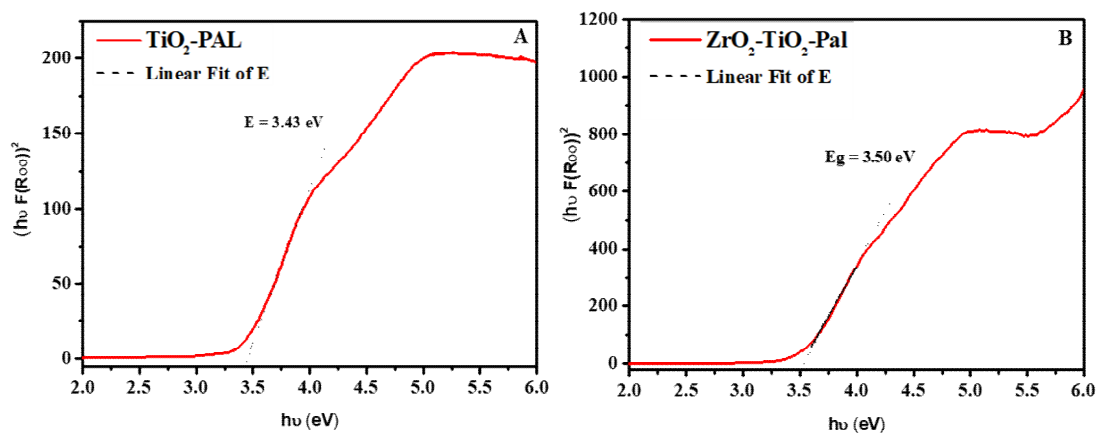


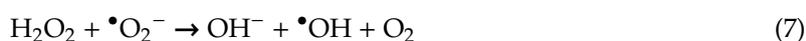
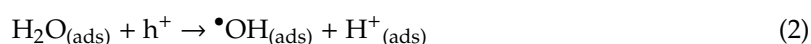
Figure 5. Kubelka–Munk curves of the (A) TiO_2 -Pal and (B) ZrO_2 - TiO_2 -Pal composites.

3.2. Photocatalytic Assays

The concentration of the photocatalyst is an important parameter in the oxidation and efficiency of a photocatalytic system because photocatalysis is directly related to particle aggregation [50]. The absorption of Remazol Blue dye in the UV-Vis spectrum at different concentrations in an aqueous solution is shown in Figure S1. The wavelength of 589 nm was chosen to monitor the photolysis in the solution because the UV region may change after the formation of photoproducts.

The photocatalytic assay of the synthesized materials is shown in Figure S2. TiO₂-Pal presented better photocatalytic performance than the ZrO₂-TiO₂-Pal composite. This performance is evidenced in the effect of the concentrations of the photocatalysts (Figure 6). At the lowest concentration of photoactive material (0.5 g L⁻¹), TiO₂-Pal shows a discoloration percentage of 98%, while the ZrO₂-TiO₂-Pal composite shows 71%. For other concentrations of photoactive materials, the difference is not clear, although TiO₂-Pal continues to exhibit better performance. The explanation for this fact is associated with the surface and structural semiconductor properties of each photocatalyst and the experimental conditions in the photocatalysis [50]. It is known that excess photocatalyst may cause a reduction in radiation passage due to particle aggregation and/or solution turbidity [51,52], compromising the passage of light and inhibiting discoloration. In addition, a decrease in discoloration efficiency with higher photocatalyst loading may be due to the deactivation of collision-activated molecules with ground-state molecules [53,54]. This implies that not only is the amount of catalyst important, but also that other factors have an influence on the generation of radicals in solution [55,56]. Similar behavior of the Pal/photocatalysis of dyes was also observed by Stathatos et al. [42] in the degradation of azo dye Basic Blue 41, using TiO₂/palygorskite for the degradation of methylene blue. The results showed that discoloration was achieved in 120 min under light, which was attributed to the synergistic effect between clay and TiO₂ [42]. In addition, considering the low amount of immobilized TiO₂, the composite formed was highly efficient in degrading the organic dye. According to Stathatos et al. [42], Pal has low photocatalytic response in UV light, probably due to the presence of light-activated oxides, facilitating the hydroxylation of the surface of these oxides to favor the recombination of charges.

The photocatalytic changes can be explained by considering that the mechanism of degradation in the presence of oxygen may involve the participation of singlet oxygen [56]. Radical species formed during the process can react with the dye, causing dye discoloration. Therefore, the photocatalytic efficiency can be understood through direct and indirect mechanisms [50,57], through the production of electrons and holes generated by photocatalyst photo-oxidation, and the interaction of these pairs that are responsible for the intermediate steps that occur in the reaction medium. Oxidation of the organic molecule, as shown by the following Equations (1)–(9), describes the mechanism of discoloration [50,57].



Zheng et al. [58] showed that the main product of the photocatalyst surface/interface redox steps is the superoxide anion ($O_2^{\bullet-}$), which is the precursor of other reactive oxygen species (H_2O_2 and $\bullet OH$).

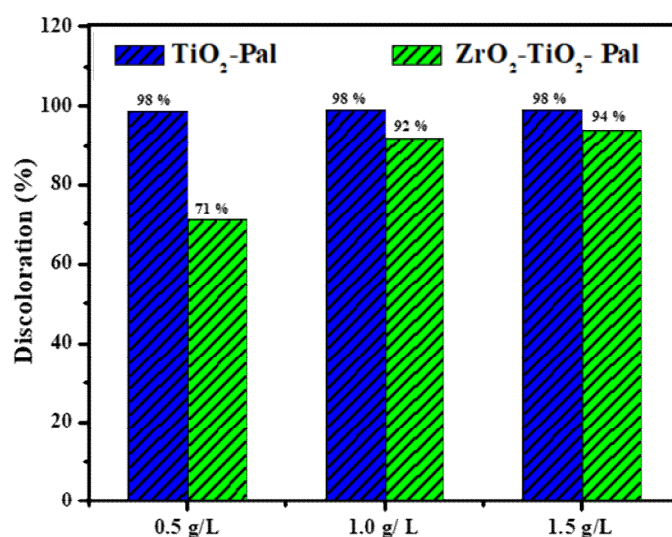


Figure 6. Discoloration percentages of Remazol Blue dye using 0.5 g L^{-1} , 1.0 g L^{-1} , and 1.5 g L^{-1} of photoactive material under UV light.

Another factor affecting the photocatalytic performance is that the TiO_2 deposited in the clay presents band gap energy of 3.43 eV, allowing electron excitation under UV radiation. This contributes to the production of photoinduced electrons and holes, producing the radicals that are responsible for the degradation process [39]. In fact, the efficiency of TiO_2 in the degradation of dyes is well known. The discoloration of Remazol Blue using a catalyst promoted the formation of different products involving electron transfer reactions and a reaction with the hydroxyl radical [59].

The deposition of zirconium into TiO_2 -Pal decreased the dye discoloration rate compared with TiO_2 -Pal for all investigated catalyst concentrations. The best Remazol Blue dye degradation was 94% at 1.5 g L^{-1} of ZrO_2 - TiO_2 -Pal. This behavior may be due to the high band gap of this material, i.e., 3.5 eV. This band gap cannot favor the production of electrons and holes under UV irradiation, resulting in the low rate of discoloration of the dye [60].

Based on the UV spectra, it is well-established that the photocatalytic kinetics of Remazol Blue follow a first-order kinetic model [59]. The reaction can be represented by Equation (10).

$$R = -dC/dt = k_r KC / (1 + KC) \quad (10)$$

where k_r is the reaction rate constant, K is the adsorption coefficient of Remazol Blue at the surface of the TiO_2 -Pal and ZrO_2 - TiO_2 -Pal composites, and C is the concentration of the dye solution. When the concentration of the dye in the solution (C) is low, the KC value is negligible in relation to unity. Therefore, Equation (10) describes a first-order kinetic model. The integration of the latter equation has the limiting condition that at the start of irradiation ($t = 0$), the concentration is initial, $C = C_0$, given by Equation (11).

$$-\ln C/C_0 = k_{app} t = k_r K t \quad (11)$$

where k_{app} is the apparent first-order reaction constant and C_0 is the initial concentration of the dye in solution. The values of the apparent first-order reaction rate constants for TiO_2 -Pal and ZrO_2 - TiO_2 -Pal are presented in Figure 7. It is important to note that only the data from the 120 min irradiation were used in the calculation of the kinetic data of the Remazol Blue dye discoloration. The k_{app} values were similar to those in other studies [59]. As expected, the apparent reaction rate

constant increased linearly with the increase in TiO_2 content. In fact, a higher TiO_2 amount implied an increase in the crystal phase and specific surface area and contributed to the photocatalytic process.

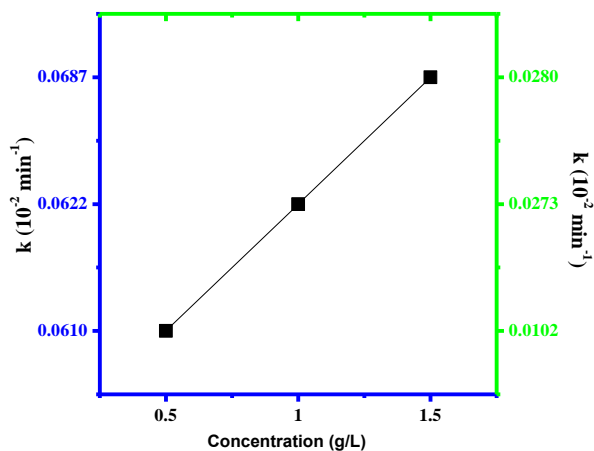


Figure 7. Rate constants of Remazol Blue discoloration in function of the photoactive materials concentration.

Effect of the Presence of SO_4^{2-} Ions

Anions/salts of different types are present in all-natural sources of water. Therefore, it is important to evaluate these anions (especially SO_4^{2-}) in water purification through photocatalytic processes [61]. The effect of the presence of 0.1 mol L^{-1} sodium sulfate was investigated in the dye discoloration in the presence of 1.5 g L^{-1} photoactive materials at 25°C . The discoloration percentages of Remazol Blue in the presence and absence of sodium sulfate in the different photoactive materials under UV light are shown in Figure 8.

The sulfate interfered with the photocatalysis assays once the discoloration rates decreased, and this behavior was even more pronounced in the $\text{ZrO}_2\text{-TiO}_2\text{-Pal}$ system. The interaction of a cationic or anionic dye molecule with the photocatalyst surface is very important in the photocatalytic process. The decrease in dye discoloration may be associated with a competition between the anionic dye and sulfate to adsorb on the positively charged surface (TiOH^{2+}) in aqueous solutions [62,63].

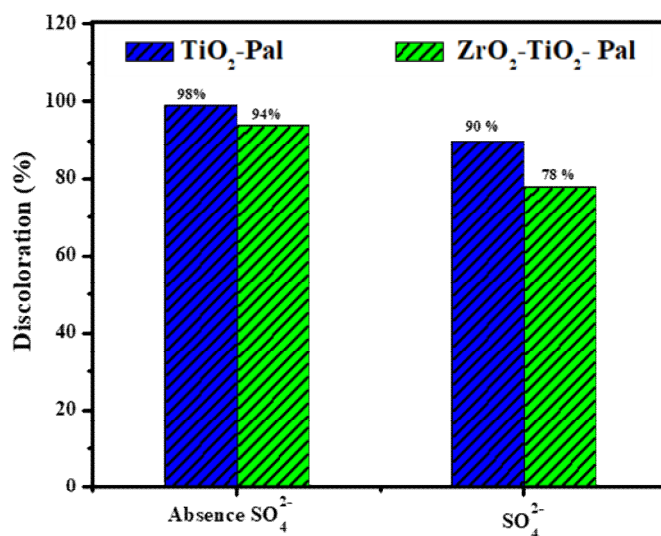


Figure 8. Discoloration percentages of the Remazol Blue using 1.5 g L^{-1} photoactive materials in the presence and absence of the sulfate ion under UV light.

In addition, the sulfate adsorbed on the surface forms a sulfate radical (see reactions with the hole (h^+) (Equation (12)) and hydroxyl radical (Equation (13)).



The sulfate radical is less reactive than $\bullet\text{OH}$, and excess SO_4^{2-} decreases the dye discoloration [62]. Therefore, the charged surface showed more affinity to SO_4^{2-} , resulting in a lower discoloration rate [64,65].

The present result is in concordance with that obtained by Zhang et al. [66], in which synthesized TiO_2 nanoparticles were immobilized on diatomite by hydrolysis deposition. The effect of sulfates on the photocatalytic activity of TiO_2 /diatomite indicated that the addition of a small amount of sulfate ions promoted the initial phase and, consequently, the stable sulfate had a strong electron affinity, capturing the photogenerated electrons and making the e^-/h^+ pair recombination difficult. Other anions and/or inorganic species have also been observed in the degradation of different pollutants [67,68].

4. Conclusions

Palygorskite was modified with nanoparticle oxides to produce a clay-based catalyst. The results showed that TiO_2 and ZrO_2 were continuously coated onto the surface of the fibrous palygorskite, thereby improving the specific surface area and narrowing the pore distribution. The synthesized TiO_2 -Pal and ZrO_2 - TiO_2 -Pal composites presented band gap energies of 3.43 eV and 3.50 eV, respectively. The system supported with TiO_2 (TiO_2 -Pal) exhibited better photocatalytic activity over UV light irradiation, independent of the semiconductor concentration used. The presence of the sulfate ion in the photocatalytic systems decreased the Remazol Blue dye degradation, which was attributed to the formation of less reactive species. Among the catalysts, TiO_2 -Pal showed the best performance for reactive dye discoloration in aqueous solution.

Supplementary Materials: The following are available online at <http://www.mdpi.com/2075-163X/10/2/132/s1>, Figure S1: UV-Visible absorption spectra for (a) Remazol Blue dye at different concentrations; (b) Photolysis of $1.0 \times 10^{-4} \text{ mol L}^{-1}$ Remazol Blue; Figure S2: (a) Dye concentration as a function of light exposure time using 0.5 g of TiO_2 -Pal or ZrO_2 - TiO_2 -Pal photoactive material, (b) UV-VIS spectra of the solution after photocatalysis of Remazol Blue using TiO_2 -Pal.

Author Contributions: Conceptualization, M.O.M. and L.M.H.; Methodology, M.O.M.; Formal Analysis, J.A.O.; Investigation, M.O.M.; Resources, all; Writing—Original Draft Preparation, M.O.M.; L.M.H. and P.T.; Writing—Review & Editing, M.G.F., B.C.V., F.F., J.A.O. and E.C.S.-F.; Visualization, all; Supervision, J.A.O. and E.C.S.-F.; Project Administration, J.A.O. and E.C.S.-F.; All authors have read and agreed to the published version of the manuscript.

Funding: This research was funded by CNPq [Brazilian National Council for Scientific and Technological], grant number [307460/2016-9].

Acknowledgments: The authors thank Coordination of Superior Level Staff Improvement (CAPES), Piauı State Research Support Foundation (FAPEPI), Brazilian National Council for Scientific and Technological (CNPQ), Federal University of Piauı (UFPI), Federal University of Paraıba (UFPB) and Universidad de Malaga.

Conflicts of Interest: The authors declare no conflict of interest.

References

1. Abhilash, P.C.; Singh, N. Pesticide use and application: An Indian scenario. *J. Hazard. Mater.* **2009**, *165*, 1–12. [CrossRef]
2. Sen Kavurmaci, S.; Bekbolet, M. Photocatalytic degradation of humic acid in the presence of montmorillonite. *Appl. Clay Sci.* **2013**, *75–76*, 60–66. [CrossRef]
3. Liu, L.; Zhang, J.; Tan, Y.; Jiang, Y.; Hu, M.; Li, S.; Zhai, Q. Rapid decolorization of anthraquinone and triphenylmethane dye using chloroperoxidase: Catalytic mechanism, analysis of products and degradation route. *Chem. Eng. J.* **2014**, *244*, 9–18. [CrossRef]

4. Pielesz, A.; Baranowska, I.; Rybak, A.; Włochowicz, A. Detection and determination of aromatic amines as products of reductive splitting from selected azo dyes. *Ecotoxicol. Environ. Saf.* **2002**, *53*, 42–47. [[CrossRef](#)] [[PubMed](#)]
5. Silva, L.S.; Lima, L.C.B.; Silva, F.C.; Matos, J.M.E.; Santos, M.R.M.C.; Santos Júnior, L.S.; Sousa, K.S.; da Silva Filho, E.C. Dye anionic sorption in aqueous solution onto a cellulose surface chemically modified with aminoethanethiol. *Chem. Eng. J.* **2013**, *218*, 89–98. [[CrossRef](#)]
6. Vidal, J.; Huiliñir, C.; Santander, R.; Silva-Agredo, J.; Torres-Palma, R.A.; Salazar, R. Effective removal of the antibiotic Nafcillin from water by combining the Photoelectro-Fenton process and Anaerobic Biological Digestion. *Sci. Total Environ.* **2018**, *624*, 1095–1105. [[CrossRef](#)]
7. Osajima, J.A.; Coelho, K. Photolysis and photocatalysis of Bentazon herbicide. *Int. J. Agric. Environ. Res.* **2016**, *2*, 843–856.
8. Clark, K.K.; Mezyk, S.P.; Abbott, A.; Kiddle, J.J. Kinetic studies of the AOP radical-based oxidative and reductive destruction of pesticides and model compounds in water. *Chemosphere* **2018**, *197*, 193–199. [[CrossRef](#)]
9. Bouna, L.; Rhouta, B.; Maury, F. Physicochemical study of photocatalytic activity of TiO₂ supported palygorskite clay mineral. *Int. J. Photoenergy* **2013**, *2013*, 815473. [[CrossRef](#)]
10. Huo, C.; Yang, H. Preparation and enhanced photocatalytic activity of Pd-CuO/palygorskite nanocomposites. *Appl. Clay Sci.* **2013**, *74*, 87–94. [[CrossRef](#)]
11. De Morais, J.L.; Zamora, P.P. Use of advanced oxidation processes to improve the biodegradability of mature landfill leachates. *J. Hazard. Mater.* **2005**, *123*, 181–186. [[CrossRef](#)] [[PubMed](#)]
12. Xu, C.; Gu, F.L.; Wu, H. BiOCl-montmorillonite as a photocatalyst for highly efficient removal of Rhodamine B and Orange G: Importance of the acidity and dissolved oxygen. *Appl. Clay Sci.* **2017**, *147*, 28–35. [[CrossRef](#)]
13. Quan, G.; Kong, L.; Lan, Y.; Yan, J.; Gao, B. Removal of acid orange 7 by surfactant-modified iron nanoparticle supported on palygorskite: Reactivity and mechanism. *Appl. Clay Sci.* **2018**, *152*, 173–182. [[CrossRef](#)]
14. Ma, J.; Zhu, C.; Lu, J.; Liu, H.; Huang, L.; Chen, T.; Chen, D. Catalytic degradation of gaseous benzene by using TiO₂/goethite immobilized on palygorskite: Preparation, characterization and mechanism. *Solid State Sci.* **2015**, *49*, 1–9. [[CrossRef](#)]
15. Nakata, K.; Ochiai, T.; Murakami, T.; Fujishima, A. Photoenergy conversion with TiO₂ photocatalysis: New materials and recent applications. *Electrochim. Acta* **2012**, *84*, 103–111. [[CrossRef](#)]
16. Zhou, F.; Yan, C.; Wang, H.; Zhou, S.; Komarneni, S. Sepiolite-TiO₂ nanocomposites for photocatalysis: Synthesis by microwave hydrothermal treatment versus calcination. *Appl. Clay Sci.* **2017**, *146*, 246–253. [[CrossRef](#)]
17. Lin, S.; Sun, S.; Shen, K.; Tan, D.; Zhang, H.; Dong, F.; Fu, X. Photocatalytic microreactors based on nano TiO₂-containing clay colloidosomes. *Appl. Clay Sci.* **2018**, *159*, 42–49. [[CrossRef](#)]
18. Gu, N.; Gao, J.; Li, H.; Wu, Y.; Ma, Y.; Wang, K. Montmorillonite-supported with Cu₂O nanoparticles for damage and removal of *Microcystis aeruginosa* under visible light. *Appl. Clay Sci.* **2016**, *132–133*, 79–89. [[CrossRef](#)]
19. Tsai, Y.-L.; Chang, P.-H.; Gao, Z.-Y.; Xu, X.-Y.; Chen, Y.-H.; Wang, Z.-H.; Chen, X.-Y.; Yang, Z.-Y.; Wang, T.-H.; Jean, J.-S.; et al. Amitriptyline removal using palygorskite clay. *Chemosphere* **2016**, *155*, 292–299. [[CrossRef](#)]
20. Rusmin, R.; Sarkar, B.; Tsuzuki, T.; Kawashima, N.; Naidu, R. Removal of lead from aqueous solution using superparamagnetic palygorskite nanocomposite: Material characterization and regeneration studies. *Chemosphere* **2017**, *186*, 1006–1015. [[CrossRef](#)]
21. Li, Z.; Fitzgerald, N.M.; Jiang, W.T.; Lv, G. Palygorskite for the uptake and removal of pharmaceuticals for wastewater treatment. *Process Saf. Environ. Prot.* **2016**, *101*, 80–87. [[CrossRef](#)]
22. Middea, A.; Spinelli, L.S.; Souza, F.G.; Neumann, R.; Gomes, O.D.F.M.; Fernandes, T.L.A.P.; De Lima, L.C.; Barthem, V.M.T.S.; De Carvalho, F.V. Synthesis and characterization of magnetic palygorskite nanoparticles and their application on methylene blue removal from water. *Appl. Surf. Sci.* **2015**, *346*, 232–239. [[CrossRef](#)]
23. Shi, Y.; Yang, Z.; Wang, B.; An, H.; Chen, Z.; Cui, H. Adsorption and photocatalytic degradation of tetracycline hydrochloride using a palygorskite-supported Cu₂O-TiO₂ composite. *Appl. Clay Sci.* **2016**, *119*, 311–320. [[CrossRef](#)]
24. Shi, Y.; Zhang, Q.; Zhu, X.; Wang, J.; Chen, J.; Shi, Y.; Yang, Z.; Cui, H.; Hu, Y.; Zhang, L.; et al. Palygorskite supported BiVO₄ photocatalyst for tetracycline hydrochloride removal. *Appl. Clay Sci.* **2017**, *137*, 249–258. [[CrossRef](#)]

25. Hoffmann, M.R.; Martin, S.T.; Choi, W.; Bahnemann, D.W. Environmental applications of semiconductor photocatalysis. *Chem. Rev.* **1995**, *95*, 69–96. [[CrossRef](#)]
26. Kwok, C.; Aita, C.R. Near-band gap optical behavior of sputter deposited α - and $\alpha + \beta$ - ZrO₂ films. *J. Appl. Phys.* **1989**, *66*, 2756–2758. [[CrossRef](#)]
27. Frost, R.L.; Xi, Y.; He, H. Synthesis, characterization of palygorskite supported zero-valent iron and its application for methylene blue adsorption. *J. Colloid Interface Sci.* **2010**, *341*, 153–161. [[CrossRef](#)]
28. Vdovic, N.; Jurina, I.; Škapin, S.D.; Sondi, I. The surface properties of clay minerals modified by intensive dry milling—Revisited. *Appl. Clay Sci.* **2010**, *48*, 575–580. [[CrossRef](#)]
29. Sarabadian, M.; Bashiri, H.; Mousavi, S.M. Adsorption of crystal violet dye by zeolite-montmorillonite: Modeling, kinetic and equilibrium studies. *Clay Miner.* **2019**, 1–45. [[CrossRef](#)]
30. Trigueiro, P.; Pedetti, S.; Rigaud, B.; Balme, S.; Janot, J.-M.; dos Santos, I.M.G.; Gougeon, R.; Fonseca, M.G.; Georgelin, T.; Jaber, M. Going through the wine fining: Intimate dialogue between organics and clays. *Colloids Surf. B Biointerfaces* **2018**, *166*, 79–88. [[CrossRef](#)]
31. Belver, C.; Bedia, J.; Rodriguez, J.J. Zr-doped TiO₂ supported on delaminated clay materials for solar photocatalytic treatment of emerging pollutants. *J. Hazard. Mater.* **2017**, *322*, 233–242. [[CrossRef](#)] [[PubMed](#)]
32. Belver, C.; Bedia, J.; Álvarez-Montero, M.A.; Rodriguez, J.J. Solar photocatalytic purification of water with Ce-doped TiO₂/clay heterostructures. *Catal. Today* **2016**, *266*, 36–45. [[CrossRef](#)]
33. Chen, H.; Wang, A. Kinetic and isothermal studies of lead ion adsorption onto palygorskite clay. *J. Colloid Interface Sci.* **2007**, *307*, 309–316. [[CrossRef](#)] [[PubMed](#)]
34. Rodrigues, L.A.S.; Figueiras, A.; Veiga, F.; de Freitas, R.M.; Nunes, L.C.C.; da Silva Filho, E.C.; da Silva Leite, C.M. The systems containing clays and clay minerals from modified drug release: A review. *Colloids Surf. B Biointerfaces* **2013**, *103*, 642–651. [[CrossRef](#)]
35. Miranda, M.O.; de Araújo, F.P.; Osajima, J.A.; Silva Filho, E.C. Incorporation of zirconium oxide on the surface of palygorskite clay for photodegradation of industrial dye. *Mater. Sci. Forum* **2016**, *869*, 768–772. [[CrossRef](#)]
36. Zhang, L.; Liu, J.; Tang, C.; Lv, J.; Zhong, H.; Zhao, Y.; Wang, X. Palygorskite and SnO₂-TiO₂ for the photodegradation of phenol. *Appl. Clay Sci.* **2011**, *51*, 68–73. [[CrossRef](#)]
37. Yuan, P.; Yin, X.; He, H.; Yang, D.; Wang, L.; Zhu, J. Investigation on the delaminated-pillared structure of TiO₂-PILC synthesized by TiCl₄ hydrolysis method. *Microporous Mesoporous Mater.* **2006**, *93*, 240–247. [[CrossRef](#)]
38. Idakiev, V.; Tabakova, T.; Naydenov, A.; Yuan, Z.Y.; Su, B.L. Gold catalysts supported on mesoporous zirconia for low-temperature water-gas shift reaction. *Appl. Catal. B Environ.* **2006**, *63*, 178–186. [[CrossRef](#)]
39. Chen, D.; Du, Y.; Zhu, H.; Deng, Y. Synthesis and characterization of a microfibrillar TiO₂-CdS/palygorskite nanostructured material with enhanced visible-light photocatalytic activity. *Appl. Clay Sci.* **2014**, *87*, 285–291. [[CrossRef](#)]
40. Grudzien, R.M.; Grabicka, B.E.; Jaroniec, M. Effect of organosilane/polymer ratio on adsorption properties of periodic mesoporous ethane-silica. *Colloids Surf. A Physicochem. Eng. Asp.* **2007**, *300*, 235–244. [[CrossRef](#)]
41. Silva, G.T.M.; Silva, C.P.; Gehlen, M.H.; Oake, J.; Bohne, C.; Quina, F.H. Organic/inorganic hybrid pigments from flavylum cations and palygorskite. *Appl. Clay Sci.* **2018**, *162*, 478–486. [[CrossRef](#)]
42. Stathatos, E.; Papoulis, D.; Aggelopoulos, C.A.; Panagiotaras, D.; Nikolopoulou, A. TiO₂/palygorskite composite nanocrystalline films prepared by surfactant templating route: Synergistic effect to the photocatalytic degradation of an azo-dye in water. *J. Hazard. Mater.* **2012**, *211–212*, 68–76. [[CrossRef](#)] [[PubMed](#)]
43. Dali Youcef, L.; Belaroui, L.S.; López-Galindo, A. Adsorption of a cationic methylene blue dye on an Algerian palygorskite. *Appl. Clay Sci.* **2019**, *179*, 105145. [[CrossRef](#)]
44. Pan, J.; Zou, X.; Wang, X.; Guan, W.; Yan, Y.; Han, J. Selective recognition of 2,4-dichlorophenol from aqueous solution by uniformly sized molecularly imprinted microspheres with β -cyclodextrin/attapulgite composites as support. *Chem. Eng. J.* **2010**, *162*, 910–918. [[CrossRef](#)]
45. Franco, F.; Pozo, M.; Cecilia, J.A.; Benítez-Guerrero, M.; Pozo, E.; Martín Rubí, J.A. Microwave assisted acid treatment of sepiolite: The role of composition and “crystallinity”. *Appl. Clay Sci.* **2014**, *102*, 15–27. [[CrossRef](#)]
46. Chahi, A.; Petit, S.; Decarreau, A. Infrared evidence of dioctahedral-trioctahedral site occupancy in palygorskite. *Clays Clay Miner.* **2002**, *50*, 306–313. [[CrossRef](#)]

47. Qi, Z.; Ye, H.; Xu, J.; Peng, J.; Chen, J.; Guo, B. Synthesis and characterizations of attapulgite reinforced branched poly (butylene succinate) nanocomposites. *Colloids Surf. A Physicochem. Eng. Asp.* **2013**, *436*, 26–33. [[CrossRef](#)]
48. Ma, J.; Zou, J.; Li, L.; Yao, C.; Kong, Y.; Cui, B.; Zhu, R.; Li, D. Nanocomposite of attapulgite–Ag₃PO₄ for Orange II photodegradation. *Appl. Catal. B Environ.* **2014**, *144*, 36–40. [[CrossRef](#)]
49. Kim, C.S.; Jeong, H.D. Band gap tuning in nanoporous TiO₂-ZrO₂ hybrid thin films. *Bull. Korean Chem. Soc.* **2007**, *28*, 2333–2337.
50. Rauf, M.A.; Meetani, M.A.; Hisaindee, S. An overview on the photocatalytic degradation of azo dyes in the presence of TiO₂ doped with selective transition metals. *Desalination* **2011**, *276*, 13–27. [[CrossRef](#)]
51. Rezaei, M.; Habibi-Yangjeh, A. Simple and large scale refluxing method for preparation of Ce-doped ZnO nanostructures as highly efficient photocatalyst. *Appl. Surf. Sci.* **2013**, *265*, 591–596. [[CrossRef](#)]
52. Papoulis, D.; Komarneni, S.; Nikolopoulou, A.; Tsolis-Katagas, P.; Panagiotaras, D.; Kacandes, H.G.; Zhang, P.; Yin, S.; Sato, T.; Katsuki, H. Palygorskite- and Halloysite-TiO₂ nanocomposites: Synthesis and photocatalytic activity. *Appl. Clay Sci.* **2010**, *50*, 118–124. [[CrossRef](#)]
53. Konstantinou, I.K.; Albanis, T.A. TiO₂-assisted photocatalytic degradation of azo dyes in aqueous solution: Kinetic and mechanistic investigations: A review. *Appl. Catal. B Environ.* **2004**, *49*, 1–14. [[CrossRef](#)]
54. Neppolian, B.; Choi, H.C.; Sakthivel, S.; Arabindoo, B.; Murugesan, V. Solar light induced and TiO₂ assisted degradation of textile dye reactive blue 4. *Chemosphere* **2002**, *46*, 1173–1181. [[CrossRef](#)]
55. Egerton, T.A.; Purnama, H. Does hydrogen peroxide really accelerate TiO₂ UV-C photocatalyzed decolouration of azo-dyes such as Reactive Orange 16? *Dye. Pigment.* **2014**, *101*, 280–285. [[CrossRef](#)]
56. Santos, W.G.; Tominaga, T.T.; Nascimento, O.R.; Schmitt, C.C.; Neumann, M.G. Phototransients of 2-ethylaminodiphenylborinate generated by direct photolysis and photosensitization. *J. Photochem. Photobiol. A Chem.* **2012**, *236*, 14–20. [[CrossRef](#)]
57. Rauf, M.A.; Ashraf, S.S. Fundamental principles and application of heterogeneous photocatalytic degradation of dyes in solution. *Chem. Eng. J.* **2009**, *151*, 10–18. [[CrossRef](#)]
58. Zheng, W.; Zou, H.-F.; Lv, S.-W.; Lin, Y.-H.; Wang, M.; Yan, F.; Sheng, Y.; Song, Y.-H.; Chen, J.; Zheng, K.-Y. The effect of nano-TiO₂ photocatalysis on the antioxidant activities of Cu, Zn-SOD at physiological pH. *J. Photochem. Photobiol. B Biol.* **2017**, *174*, 251–260. [[CrossRef](#)]
59. Saquib, M.; Muneer, M. Semiconductor mediated photocatalysed degradation of an anthraquinone dye, Remazol Brilliant Blue R under sunlight and artificial light source. *Dye. Pigment.* **2002**, *53*, 237–249. [[CrossRef](#)]
60. Chang, J.P.; Lin, Y.S.; Chu, K. Rapid thermal chemical vapor deposition of zirconium oxide for metal-oxide-semiconductor field effect transistor application. *J. Vac. Sci. Technol. B Microelectron. Nanom. Struct.* **2001**, *19*, 1782–1787. [[CrossRef](#)]
61. Gayathri, P.V.; Yesodharan, S.; Yesodharan, E.P. Microwave/Persulfate assisted ZnO mediated photocatalysis (MW/PS/UV/ZnO) as an efficient advanced oxidation process for the removal of RhB dye pollutant from water. *J. Environ. Chem. Eng.* **2019**, *7*, 103122. [[CrossRef](#)]
62. Lim, J.; Kwak, D.-Y.; Sieland, F.; Kim, C.; Bahnemann, D.W.; Choi, W. Visible light-induced catalytic activation of peroxymonosulfate using heterogeneous surface complexes of amino acids on TiO₂. *Appl. Catal. B Environ.* **2018**, *225*, 406–414. [[CrossRef](#)]
63. Nasirian, M.; Mehrvar, M. Photocatalytic degradation of aqueous Methyl Orange using nitrogen-doped TiO₂ photocatalyst prepared by novel method of ultraviolet-assisted thermal synthesis. *J. Environ. Sci. (China)* **2018**, *66*, 81–93. [[CrossRef](#)] [[PubMed](#)]
64. Turolla, A.; Bestetti, M.; Antonelli, M. Optimization of heterogeneous photoelectrocatalysis on nanotubular TiO₂ electrodes: Reactor configuration and kinetic modelling. *Chem. Eng. Sci.* **2018**, *182*, 171–179. [[CrossRef](#)]
65. Hu, C.; Yu, J.C.; Hao, Z.; Wong, P.K. Effects of acidity and inorganic ions on the photocatalytic degradation of different azo dyes. *Appl. Catal. B Environ.* **2003**, *46*, 35–47. [[CrossRef](#)]
66. Zhang, J.; Wang, X.; Wang, J.; Wang, J.; Ji, Z. Effect of sulfate ions on the crystallization and photocatalytic activity of TiO₂/diatomite composite photocatalyst. *Chem. Phys. Lett.* **2016**, *643*, 53–60. [[CrossRef](#)]

67. Abdel-Khalek, A.A.; Mahmoud, S.A.; Zaki, A.H. Visible light assisted photocatalytic degradation of crystal violet, bromophenol blue and eosin Y dyes using AgBr–ZnO nanocomposite. *Environ. Nanotechnol. Monit. Manag.* **2018**, *9*, 164–173. [[CrossRef](#)]
68. Wang, C.; Xue, Y.; Wang, P.; Ao, Y. Effects of water environmental factors on the photocatalytic degradation of sulfamethoxazole by AgI/UiO-66 composite under visible light irradiation. *J. Alloys Compd.* **2018**, *748*, 314–322. [[CrossRef](#)]



© 2020 by the authors. Licensee MDPI, Basel, Switzerland. This article is an open access article distributed under the terms and conditions of the Creative Commons Attribution (CC BY) license (<http://creativecommons.org/licenses/by/4.0/>).